This is a preprint, the final version is subject to change, of the American Mineralogist (MSA)
Cite as Authors (Year) Title. American Mineralogist, in press.
(DOI will not work until issue is live.) DOI: http://dx.doi.org/10.2138/am.2014.4545

Revision 4

Comparison of metal enrichment in pyrite framboids from a metal-enriched and metal-poor estuary

Daniel Gregory[1], Sebastien Meffre[1] and Ross Large[1]

[1]: CODES ARC Centre of Excellence in Ore Deposits, Private Bag 126, University of Tasmania, Australia, 7001

Corresponding author: Daniel Gregory (ddg@utas.edu.au)

Abstract

The accumulation of metals and metalloids in diagenetic pyrite framboids is of interest because framboids can be a sink for heavy metal contaminants, a source of metals in ore deposits, and a tool to interpret paleo-ocean chemistry. In this study we have used laser ablation inductively coupled plasma mass spectrometry (LA-ICPMS) to analyze pyrite framboids from both the contaminated Derwent Estuary and the uncontaminated Huon Estuary in Tasmania, Australia. While the enrichment of many trace metals in the Huon Estuary followed expected trends, the trends in the Derwent were quite different. In addition to the expected high contents of Pb, Zn and Cu in the contaminated interval it was found that a number of elements are incorporated into pyrite less within the contaminated zone. It is suggested that this is due to over competition for adsorption sites on the growing iron sulfides in the contaminated zone resulting in diffusion of several elements down. This results in an increase of these elements in pyrite below the zone of major contamination. The LA-ICPMS technique also provided the opportunity to obtain accurate data on gold, silver and tellurium in diagenetic pyrite, something rarely achieved in sequential leach extractions due to the low concentrations of these metals observed in nature.

Keywords

Diagenetic, pyrite, trace metals, framboid, metal contamination, LA-ICPMS

Introduction

Metal and metalloid accumulation in sediments has recently become of interest for three main reasons. Firstly, pyrite framboids can be important sinks for metals and metalloids (such as As) in contaminated rivers and estuaries (Lowers et al., 2007). Secondly, trace metal contents of shale can be used to interpret paleo-environmental conditions (Algeo, 2004; Anbar et al., 2007; Berner et al., 2013; Tribovillard et al., 2006) and since diagenetic pyrite is one of the sinks for trace metals in sediments (Dellwig et al., 2002; Huerta-Diaz and Morse, 1992; Neumann et al., 2013), the processes that led to enrichment of trace metals in pyrite are important. Thirdly, recent ore deposit models suggest that diagenetic pyrite is the source for several significant gold deposits (Large et al., 2007, 2009; Thomas et al., 2011). It is therefore important to gain some understanding of the factors that control the uptake of trace elements in pyrite. Previous studies have used partial digestions (Huerta-Diaz and Morse, 1992) to establish the variations of metal content in diagenetic pyrite according to sediment depth. While this is a useful technique for studying at uncontaminated sediments, there are many potential problems including the specificity of the reagents (Martin et al., 1987). This is of particular concern in contaminated estuaries where there may be other metal bearing sulfides (e.g. sphalerite, chalcopyrite, and galena) which dissolve under similar conditions to pyrite.

This study examines pyrite samples from a metal-enriched site in the Derwent Estuary in Tasmania and compares them to the pyrite formed in an uncontaminated environment in the Huon Estuary some 45 km to the south to determine relative affinities of different trace metals for incorporation in framboidal pyrite. To avoid problems associated with specificity

of reagents in partial digestion chemical analyses we employ LA-ICPMS analyses to directly determine the composition of trace metals in pyrite. To achieve similar results synchrotron µ-XRF has been used to analyze trace element content of pyrite (Berner et al., 2006; Neumann et al., 2013). While synchrotron µ-XRF is preferable due to its superior detection limits and spatial resolution we show in this paper that LA-ICPMS is a useful technique provided that the framboids analysed are large enough to obtain an adequate signal.

Trace element incorporation into diagenetic pyrite

The iron sulfides examined in this study are pyrite framboids, which are clusters (often spherical) of microcrystalline pyrite rarely over 15µm in diameter (Figure 1). These crystals form throughout the world in sediments under anoxic to euxinic conditions. The mechanism of framboid formation has been the subject of much research and debate (Schoonen, 2004). The process begins with the formation of iron monosulfides, which have a much higher rate of nucleation, effectively prohibiting the direct precipitation of pyrite unless seed crystals of pyrite are present (Schoonen and Barnes, 1991). These iron monosulfides are then converted to the more thermodynamically stable pyrite (Rickard and Luther, 1997). A common FeS species used in experimental studies is mackinawite (FeS_m) (Lennie et al., 1995; Wolthers et al., 2003). However, FeS_m may not be a necessary precursor in many natural systems and is only observed in systems with high Fe concentrations (Rickard and Luther, 2007), though as the system examined in this study has a significant Fe supply (Risdon Zn smelter) FeS_m was probably present at one stage. The conversion of FeS to FeS_2 can be enhanced by the presence of sulphur species with oxidation states between SO_4^{2-} and H_2S^{2-} which can be common near the reduced sediment / oxidized water column interface (Neumann et al., 2005).

Bacteria can play a role in converting organic sulfur compounds to reactants that can take part in pyrite formation (Donald and Southam, 1999; Schoonen, 2004). Microorganisms can also provide anionic sites on their cell walls that are capable of binding ferric iron (Donald and Southam, 1999; Konhauser, 1998). These ferric iron binding sites promote the growth of a thin FeS film on the outside of the cell wall (Schoonen, 2004), which then can react to form pyrite. Pyrite precipitation may also be enhanced by the presence of an active surface that allows Fe^{2+} to react with S_2(-II) to form pyrite. Other Fe sulfides (such as mackinawite) and/or organic surfaces may also fulfill this role (Rickard and Luther, 2007).

The mechanisms for the incorporation of trace metals into pyrite framboids are still not fully understood. Work by Morse and Arakaki (1993) showed that many trace metals can be adsorbed and incorporated into the precursor FeS mineral, mackinawite. They showed that a metal with a sulfide species that has a higher solubility than mackinawite would have a similar surface affinity to mackinawite and a metal with a sulfide species with lower solubility than mackinawite would have a higher surface affinity with decreasing metal sulfide solubility. Renock et al. (2009) showed that the mechanism of arsenic precipitation onto mackinawite differs based on the pH of the solution. Arsenic forms “realgar like” As sulfide minerals on the surface of mackinawite at pH 5 but at pH 9 it instead forms a coating of arsenic on the surface of the mackinawite, possibly due to adsorption of As oxyanions (Renock et al., 2009). However, mackinawite is not a long lived species and reaction pathways to convert mackinawite to pyrite proposed by (Rickard and Luther, 1997) require its dissolution, which would likely release some of the trace metals. Work by Huerta-Diaz and Morse (1992) showed that as progressively more mackinawite is converted to pyrite a greater concentration of transition metals (excluding Cr) are incorporated into the structure of pyrite. This process is limited only by the amount of pyrite produced and the amount of trace metals available to be added to the pyrite. They also found that, although metals such as Cr,

Zn, Pb and Cd do exhibit increases as more of the reactive iron is converted into pyrite (i.e. with increasing degree of pyritization), the increases are not as significant as with the other transition metals. This may be because these elements are not held within the structure of the pyrite.

Based on their study of the Lower Toarcian Posidonia Shale, Berner et al. (2013) separated trace elements in pyrite into four groups: heavy metals (Cu, Ni, Co, Pb, Bi and Tl); oxyanionic elements (As, Mo and Sb); elements that are predominantly in sub-microscopic sphalerite inclusions (Zn and Cd) and elements that occur in micro-inclusions of organic matter or silicates (Ga and V). Berner et al. (2013) and Dellwig et al.(2002) have shown that heavy metals tend to be incorporated in pyrite predominantly during diagenesis of anoxic sediments. This occurs by a number of different processes: co-precipitation; chemical or physical adsorption and redox reactions between dissolved species and the pyrite surface or the surface of pyrite precursors.

In this study LA-ICPMS was used to analyze individual pyrite framboids and determine their trace metal and metalloid abundance. This is an improvement over sequential extraction techniques of analyzing pyrite as it does not have the problems of selectivity of reactants that were identified by Martin et al. (1987). By avoiding the problem of selectivity of reactants it was possible to examine pyrite framboids that were growing in an area that contains high levels of several trace elements to examine how trace elements are incorporated into diagenetic pyrite. This is the first study to analyze the accumulation of elements in pyrite framboids from a heavily contaminated site and gives insight into the importance of competition for adsorptive sites on the surface of growing pyrite grains for the incorporation of metals within diagenetic pyrite.

Material and Methods

Location and setting

Samples were taken from two estuaries in southern Tasmania, Australia. A sediment core from the Derwent Estuary, (Figure 2) (Gregory et al., 2013) was taken from Prince of Wales Bay, adjacent to the Risdon zinc refinery which has been operating since 1917. Prior to the 1970's little environmental precautions were taken; smelter waste was deposited directly into the estuary and ore particles were blown into the water from uncovered stockpiles on the river bank (Gregory et al., 2013). In 2010 the Australian national pollution inventory reported 99 kg As, 311 kg Cd, 299 kg Cu, 654 kg Pb and 23834 kg Zn were deposited into the estuary (Milne, 2012).

The Huon Estuary is located approximately south-southwest of the Derwent Estuary at 43° 14' S and 147° 4' E. The Huon Estuary has similar underlying geology to the Derwent and drains a hinterland of mixed forest and farming areas. In comparison to the Derwent the Huon Estuary is sparsely populated and hosts few major industries on its margins and is therefore a low contamination analogue of the Derwent Estuary (Jones et al., 2003).

Sample collection and preparation

A 1.05 m sediment core taken from Prince of Wales bay (42°49'33"S, 147°18'12"E) in August 2010 and a 0.65 m long sediment core taken from the Huon Estuary (43°10'26"S, 146°59'7"E) in December 2011 were both sampled using an Uwitec hammer corer (Figure 2). The black silt found in both cores (predominantly 2.5Y 2.5/1 with zones of 5Y 2.5/1 on the Munsell colour chart) contained nearly no stratification and exhibited strong evidence of bioturbation by worms and arthropods. The sediment was extruded by pushing a plunger through the tube and samples were taken every 2.5 cm for the first 30 cm of the Derwent sediment core and 5 cm for the remainder of the cores. One half of each sample was dried prior to processing for geochemical analysis; one quarter was removed for heavy mineral

separation while the remaining quarter was stored in a freezer for future use. Heavy minerals were separated by either panning or by heavy liquid separation (heavy liquid separation was only used for the Derwent samples). The samples were first panned using a plastic riffled pan. The concentrate was then transferred to a watch glass which was further panned to produce a concentrated separate of heavy minerals. Individual pyrite framboids were removed from the concentrate using a steel needle. Framboids were then mounted in 2.5 cm diameter epoxy mounts prior to LA-ICPMS analysis. Heavy mineral separates were also made by mixing the sediment sample with lithium heteropolytungstates in a separatory funnel and leaving for 24 hrs. The dense minerals (>2.95 specific gravity) settled to the bottom of the funnel where they were collected by opening the valve and draining the bottom fraction of the lithium heteropolytungstates with the dense minerals. The minerals were filtered out and washed three times with deionized water. This concentrate was mounted in epoxy for LA-ICPMS analysis. The extracted framboids tended to be 10-20 µm in diameter and were usually spherical. However pyrite was also found to replace/fill biological structures and take the shape of that structure, an partially filled example of this is shown in Figure 1A.

Analytical methods

The dried samples were ground to <63 µm using a chromium steel mill. These samples were analyzed for metal concentrations using a combination of ICPAES (Agilent 725 Radial ICPAES) and ICPMS (Perkin Elmer Elan 9000 ICPMS) techniques at ALS Chemex in Brisbane, Australia and separately for gold using the instrumental neutron activation (INAA) technique at the Ecole Polytechnique Montreal in Canada. At ALS Chemex's lab the samples were digested by four acids (HCl, HNO_3, H_2SO_4 and HF) prior to being analyzed by ICPAES and ICPMS. Only ICPAES analysed Al, Ca, Cr Fe, K, Mg, Mn, Na, P, S, V and Zn while only ICPMS analysed Ce, Cs, Ge, Hf, In, Li, Nb, Rb, Re, Sn, Ta, Te, Th and Y. Both methods analysed Ag, As, Ba, Be, Bi, Cd, Co, Cu, Ga, La, Mo, Ni, Pb, Sb, Se, Sr, Ti, Tl, U,

W and Zr and the final values were obtained by merging the results from both methods using a complex algorithm (details provide in electronic appendix). Blanks, geochemical reference materials (MRGeo02 and GBM398-1; prepared by Ore Research & Exploration Pty Ltd and Geostats Pty Ltd respectively) and sample duplicates were used to ensure quality control. These were within the criteria for acceptable values (10-20% of the expected values, with higher variation considered acceptable for elements with low expected values). Details of the Derwent samples have been reported in a companion study (Gregory et al., 2013). At the Ecole Polytechnique the samples were placed into 7 ml irradiation polyethylene vials prior to irradiation in the Slowpoke nuclear reactor, where they were irradiated for 30 min at an average neutron flux of $5 \times 10^{11}/cm^2/s$ (varying from 4.43 to $5.58 \times 10^{11}/cm^2/s$ as a function of sample position in the irradiation site). They were then allowed to decay between three and five days before the gamma ray spectrum was recorded for three to five hours at a distance of 1.6 mm. The amount of gold was then calculated using EPAA v3.0 (Ecole Polytechnique Activation Analysis) software. Over several years of analyses the reactor neutron flux and detector efficiency has been reproducible to 1% and a quality control standard containing 30 µg gold is routinely analyzed and it was within 5% of the expected value.

Analyses of available metal ions for four of the Derwent samples were conducted as part of the companion study based on the methods proposed by Zeien and Brümmer (1989). This method consisted of seven leach steps designed to release metals that are: easily exchanged, weakly complexed and bound by carbonates, bound by Mn (hydr)oxides, bound by organic matter, bound by Fe (hydr)oxides of low crystallinity, bound by Fe (hydr)oxides of high crystallinity and the residual fraction. Of these the first four leachates have been presented in this study as possibly available for incorporation into pyrite. Though it should be noted that some of the elements held within the Mn (hydr)oxides and organic matter may be unavailable

for incorporation into pyrite because they are too strongly held by the organic matter. The first four leachates were obtained by leaching the samples with: 1 M NH_4NO_3 for 24 hours at 20°C (leach 1); 1 M NH_4OAc (pH 6) for 24 hours at 20°C (leach 2); 0.1 M NH_3OHCl + NH_4OAc (pH 6) for 0.5 hours at 20°C (leach 3) and 0.025 M NH_4-EDTA (pH 4.6) for 1.5 hours at 20°C (leach 4) (Gregory et al., 2013). The resulting aliquots were analyzed in the Central Science Laboratory at the University of Tasmania using an ELEMENT 2 sector field ICP-MS (Thermo Fisher, Bremen, Germany). Quality control was undertaken by analyzing calibration solutions as 'unknowns' to monitor instrument performance and by analyzing a water standard (NIST_RefWater1640a) to verify calibration accuracy.

The metal and metalloid contents of pyrite framboids were determined using a LA-ICPMS system (a New Wave UP-193SS Nd:YAG Q-switched Laser Ablation System or a New Wave UP-213 Nd:YAG Q-switched Laser Ablation System coupled to an Agilent 7500a Quadrapole ICP-MS) based at the ARC Centre of Excellence in Ore Deposits at the University of Tasmania. Using a 10 µm beam the samples were ablated in an ultra-high purity He atmosphere before being mixed with Ar and flowing into the ICPMS. Laser energy of 1.8 to 2.5 Jcm^{-2} (for the New Wave UP-193ss) and approximately 3.5 J/cm^2 (for the New Wave UP-213) were used for all analyses while the repetition rate was 5 Hz. Data was collected over 70-90 s intervals, with a 30 s pre-ablation acquisition (background) interval and a 40-60 s acquisition interval. Generally the first 20 s of the laser signal was used for data reduction due to the tendency for the laser to completely ablate through the pyrite framboid. However, this was enough time to obtain sufficient signal to produce analyses with adequate detection limits and errors for most elements. Many of these results had relatively high detection limits for Au and Te (>0.1 ppm and >1.0 ppm respectively) and so an additional 97 samples were analyzed for a limited number of elements (Au and Te) in an attempt to lower the detection limits.

The primary standard used to calculate concentrations and correct for instrument drift was STDGL2b-2. The standard is a lithium-borate fused disc of pyrite and sphalerite powder doped with certified element solutions (Danyushevsky et al., 2011). This standard yields an error of less than 15% for most elements. The standards were analyzed twice at the beginning and end of each session, before and after each sample change and every one to two hours of analysis time. A total of 256 analyses were conducted. Iron was used as an internal standard as pyrite rarely varies from its stoichiometric value by more than 5% (Danyushevsky et al., 2011). All results were corrected for linear drift and data reduction was undertaken following the methodology developed by Longerich et al. (1996) using SILLS software (Guillong et al., 2008).

Results

Geochemistry

Results for the whole sediment analysis are summarized in Figure 3. A more comprehensive analysis of the bulk chemistry of the sediments is presented in a companion paper (Gregory et al., 2013). It is readily apparent that the Derwent samples are much more enriched than the Huon samples above 75 cm depth for all reported elements except Co, Te and Mo (Figure 3). The increase in S content with depth in the Huon samples may reflect a natural increase in the degree of pyritization in the core (i.e. the amount of reactive Fe that has been precipitated as pyrite) (Figure 3). The Derwent core sample has been divided into 5 different groups based on the geochemical results: moderate metal and low sulfur (0 to 25 cm); moderate metal and high sulfur (25 to 45 cm); high metal (45 to 55 cm); high to low metal transition zone (55 to 80 cm) and low metal (80 to 100 cm). Representative samples from four of these groups were analyzed by sequential analysis to determine what sediment components the different metals are held within (Gregory et al., 2013). Results for the amount of trace metals that may

be available for incorporation into pyrite are summarized in Table 1. These are the sum of the easily extractable fraction; carbonate held fraction; Mn(hydr)oxide fractions and organic held fraction. The poorly crystallized Fe (hydr)oxide and well crystallized Fe (hydr)oxide fractions obtained from the sequential leach extractions were not included because in the Derwent Estuary there is a high concentration of franklinite (zinc ferrite) which dissolves under the conditions used to extract the different Fe (hydr)oxide fractions (Gregory et al., 2013). This franklinite is stable in the sediments as is indicated by SEM analyses that show no alteration on the rims of the grains (Gregory et al., 2013). Thus it was believed that including analyses from these extractions would give concentrations much higher than those actually available for incorporation in the pyrite. Unfortunately degree of pyritization analyses are not possible in the Derwent Estuary due to the presence of significant quantities of Fe (hydr)oxide and sulfide minerals being introduced into the estuary as smelting by products (Gregory et al., 2013). For complete discussion on techniques used to isolate these different fractions please see Gregory et al. (2013).

During the course of this study 159 pyrite framboids were analyzed for Al, V, Co, Ni, Cu, Zn, As, Mo, Ag, Cd, Te, Au, Pb and Bi and 97 pyrite framboids were analyzed for only Au and Te using the LA-ICPMS technique. Median, maximum and minimum values for Zn, Pb, Cu, Bi, Ni, Co, Mo, As, Au, Ag and Te in pyrite for the Derwent and Huon Estuaries are reported in Table 2 and 3 respectively.

Median values for pyrite framboids from the Huon Estuary are generally uniform with concentrations of trace metals varying little with depth. Gold, Ag and Te from individual grains are generally below detection limits and medians of Zn (26 – 65 ppm), Pb (0.30 – 2.5 ppm), Bi (0.05 – 12 ppm), Ni (2.77 – 18.8 ppm), Co (0.87 – 25.7 ppm) and As (122 – 590 ppm) show little systematic variation with depth. Whereas the concentration in pyrite of Cu

(11 – 82 ppm) and Mo (below 30 cm depth) (5.3 – 40 ppm) show a significant increase with increasing depth (Figure 4).

The Zn, Pb, Cu and Bi content in pyrite framboids in the Derwent follow the trend indicated by the whole rock analyses (Figure 4), with the highest amount of metal in the framboids occurring in the most contaminated zone but with much lower content of metal within the pyrite than in the sediment itself. Arsenic in pyrite also follows the whole rock values; however it contains higher As values than the sediment. The concentration of Ag in pyrite is relatively low and uniform throughout the contaminated interval (between <0.11 ppm and 2.90 ppm from 0 to 55 cm) and are highly enriched at 70 to 75 cm (23.96 ppm), with minor enrichment at 60-65 cm. A similar peak in trace element content of pyrite in the 70 to 75 cm interval is present for Ni, Co and Mo (35.0, 83.8 and 22.1 ppm respectively) despite these elements not being noticeably enriched in any section of the core. Gold behaves similarly, however its interval of major enrichment occurs between 60 and 65 cm below the main zinc enrichment. The Te content of pyrite is not enriched at any level in the core, however it is significantly enriched compared to the Huon core despite both cores having similar bulk Te contents. Both Au and Te are enriched in pyrite compared to the bulk sediment.

The LA-ICPMS data is collected every 0.1-0.5 s as the laser ablates through the framboid and this data can help to distinguish which elements are held within the pyrites structure/micro-inclusions within the pyrite or as larger inclusions within the framboid. Elements that exhibit relatively flat traces throughout the laser ablation are thought to be contained within the structure or micro-inclusions while elements with distinct peaks are thought to exist as larger inclusions (Thomas et al., 2011). Based on these criteria As, Mn and Zn appear to be held within the pyrite structure or as micro-inclusions; Te, Au and Sb are held as inclusions and Cu, Pb and Ag are contained in the framboids as both inclusions and contained within the pyrite structure or microinclusions (Figure 5).

Discussion

Previous enquiries into the accumulation of trace elements in pyrite forming within sediments have shown that mechanisms that incorporate different trace metals into pyrite proceed at different rates. These are, in decreasing order: As = Mo > Cu = Fe > Co > Ni >> Mn > Zn > Cr = Pb > Cd (Morse and Luther, 1999). These were determined using modifications by Huerta-Diaz and Morse (1990) on the pyrite extraction method proposed by Lord (1982) to determine the percentage of different trace metals and metalloids incorporated into pyrite, termed the degree of trace metal pyritization. As this method is not selective for pyrite, it is only applicable in areas where no other sulfides or minerals with similar chemical properties to sulfides occur. Our study differs in that the LA-ICPMS technique allows us to analyze selected pyrite framboids individually which greatly expands the potential areas of study.

Incorporation of metals and metalloids occurs by a number of different ways (Rosso and Vaughan, 2006). Which of these, or combination of these, mechanisms occur for the different elements effects how much of them can be incorporated into the individual framboids and the rate of incorporation. These interactions of metals and metalloids with the surface of the growing pyrite are controlled by several factors: equilibration time, solution pH, initial concentration of elements, particle size, temperature (Borah and Senapati, 2006) and point of zero charge (Pikaray et al., 2005).

However, micro-environments with different pH or trace element concentrations may have formed locally within the sediment. The existence of these micro-environments may explain the spread that is evident for trace element content of pyrite in the same sediment interval (Hochella et al., 2005; Xia et al., 2009).

Arsenic is enriched in pyrite by approximately an order of magnitude in both the high metal content Derwent and low metal Huon Estuaries when compared to the whole rock sediment

316 analyses. The only interval where this does not hold is in the most contaminated section of
317 the Derwent core where several framboids have lower arsenic content than that measured in
318 the host sediment. This is due to much of the As being held in other phases (such as
319 arsenopyrite) in this interval that is not available for incorporation into pyrite (Figure 6). This
320 is because As readily substitutes into pyrite at a high rate; which makes incorporation into
321 pyrite the primary mechanism in which As is removed from pore water (Lowers et al., 2007).
322 This is supported by SEM analyses (Gregory et al., 2013) that show the presence of
323 arsenopyrite in the metal enriched sections of the sediment.

324 Molybdenum behaves differently than expected with several framboids displaying erratic
325 enrichment relative to the host sediment in the contaminated zone and an increase in the Mo
326 in pyrite below the contaminated zone at 70-75 cm. Molybdenum exists in the sediment as
327 the molybdate or thiomolybdate anion or one of the intermediates between these two end
328 members (Erickson and Helz, 2000; Helz et al., 1996; Xu et al., 2006). Of these, the
329 thiomolybdate anion is likely to be in highest abundance in the sulfide rich conditions of the
330 sediments (Erickson and Helz, 2000). This is also the most efficient form to adsorb onto
331 pyrite, however it is also the most efficient form to adsorb onto organic matter (Erickson and
332 Helz, 2000; Helz et al., 1996). In the Derwent samples there is significantly more organic
333 matter above 45 cm depth (Gregory et al., 2013), which is where the Mo content of pyrite is
334 comparatively low. This suggests that competition between pyrite and organic matter for
335 adsorption of Mo may be responsible for the observed lower Mo content of pyrite above 45
336 cm. In the uncontaminated Huon Estuary molybdenum holds with the predictions of Morse
337 and Luther (1999) with the medians of the Mo in pyrite above that in the host sediment. The
338 trends with depth also fit with the predictions by Huerta-Diaz and Morse (1992), which
339 predict an increasing trace metal abundance with depth; in the Huon we see this trend below
340 30 cm of sediment depth (Figure 4).

Water exchange rate kinetics for Pb and Zn are faster than that for iron which suggests that Pb and Zn sulfides should precipitate earlier than pyrite (Morse and Luther, 1999). The incorporation of these metals in pyrite is also favored under the conditions found in the saline sediments as the pH found in the sediments is above the adsorption edge for these metals on pyrite (Jean and Bancroft, 1986). Our data support this result in the Huon Estuary where the time resolved LA-ICPMS output graphs show relatively spikey compositions of Pb and Zn (Figure 5), suggesting the presence of inclusions of these elements as sulfide inclusions within the pyrite. The time resolved LA-ICPMS data from the Huon samples also indicates a decrease in the amount of Pb and Zn from the center of the framboid to the edge. This is consistent with early rapid crystallization of Pb and Zn sulfides, which are associated with the earliest growth of pyrite framboids. In the contaminated sediments of the Derwent Estuary lead and zinc behave somewhat differently with relatively consistent compositions throughout the pyrite framboid (Figure 5). This may be due to the amount of available zinc and lead (from the first four steps of the sequential leach data), which increases from 1935 ppm and 1415 ppm respectively in the 20-25 cm interval to 4750 ppm and 4645 ppm respectively in the 50-55 ppm interval (Table 1 and Figure 6). This results in the observed increase in Pb and Zn in the framboids. These metals occur most likely as several micro-inclusions that are evenly distributed throughout the framboid. Though the exact mineral that forms the nanoparticles was not determined studies by Berner et al, (2013) and Deditius et al., (2011) has shown that Zn and Pb often exist as sulfide nanoparticles in pyrite; therefore it is probable that the nanoparticles are sulfides. This inclusion hypothesis is supported by work from Deditius et al. (2011) which has shown that a wide range of nano particles are found in pyrite as native metals, sulfides, sulfo-salts and iron bearing nanoparticles. In the course of their study they showed that Pb, Bi, Sb, Au, Ag, Ni, Te and As preferentially distribute into nano particles, with large particles forming by exsolution and small ones forming by direct

366 precipitation. However, they did not investigate Zn, in this study Zn appears to behave
367 similarly to Pb and thus it is suggested that it too preferentially forms nano particles in pyrite.

368 Zinc tends to be accumulated in pyrite less than Pb and Cu, relative to the total amounts of
369 Zn, Pb and Cu in the system. This may be because the pK_1 for the formation of the $MeOH^{z-1}$
370 complexes are higher for Zn (8 for Cu, 7.7 for Pb and 9 for Zn) (Baes and Mesmer, 1976),
371 resulting in less efficient Zn adsorption (Müller et al., 2002). A wide degree of variation in
372 the content of Pb and Cu is found, especially within the most contaminated zones. This may
373 be due to competition for the same adsorption sites, similar to that noted by Müller et al.
374 (2002).

375 In our experiment Cu behaves very similarly to Pb and Zn, as predicted by water exchange
376 reaction kinetics (Morse and Luther, 1999). This is not surprising as Cu adsorption on pyrite
377 has been shown to be rapid and at pH over 5 (Wang et al., 1989). Similar to Pb and Zn, the
378 Cu in framboids from the uncontaminated Huon Estuary sediments has a spiky (inclusion-
379 rich) distribution with an overall decrease in Cu towards the rims of the framboid (Figure 5).
380 In the Derwent Estuary sediments Cu in the framboid is less spikey than in that the Huon
381 River framboids but more spikey than the Derwent Pb and Zn.

382 Gold content in pyrite was found to be subdued in the most metal enriched part of the
383 Derwent core, with the highest gold in pyrite present below the major metal enrichment. The
384 Au precipitates from pore waters either by adsorbing onto sulfides or other materials (Jean
385 and G Michael, 1985; Maddox et al., 1998; Mycroft et al., 1995; Renders and Seward, 1989;
386 Schoonen et al., 1992; Widler and Seward, 2002; Woods, 1996) or by precipitation due to
387 bacterial mediated precipitation of gold metal (Gwynne, 2013; Hough et al., 2011; Lengke et
388 al., 2006; Reith et al., 2009). Schoonen et al. (1992) showed that pyrite is a very good
389 scavenger of gold in natural systems. This is achieved by the adsorption of gold on the

surface of the growing crystals with incorporation into the structure of the pyrite by subsequent over growth. However, gold is also adsorbed by organic matter through biologic pathways (Zhang et al., 1997). The top of the sediment section in the Derwent core contains a higher amount of organic matter (Gregory et al., 2013) and in this region pyrite framboids tend to also have lower Au content. This suggests that more of the available Au is adsorbed onto organic matter resulting in less gold accumulation in pyrite. Müller et al. (2002) showed that high concentrations of Cu, Pb and Zn prevented the adsorption onto pyrite of Au in pyrite rich mine tailings. It is possible that this process is occurring in the Derwent core, where additional competition for surface adsorption sites from Pb, Zn and Cu in the contaminated zone has resulted in relatively low Au incorporation into pyrite fraction (Figure 6 and Table 1). Another possibility is that bacterial meditated precipitation of Au is enhanced at this depth. Several studies (Gwynne, 2013; Lengke et al., 2006; Reith et al., 2009) have shown that sulfate-reducing bacteria can precipitate nanoparticle Au in conditions where pyrite can be formed. We consider this mechanism to be plausible in our samples as our data show the small inclusions of Au that are expected from this mechanism and the Au nano-particle fixing bacteria (*Cupiavidus metallidures*) has been identified in Australian field sites (Reith et al., 2006).

Another factor likely to effect the uptake of Au in pyrite framboids is the presence or lack of As. Several studies have shown that coatings of As on the surface of iron sulphides greatly enhance the adsorption of Au on pyrite and higher As concentrations are often associated with higher Au concentrations (Deditius et al., 2008; Deditius et al., 2009; Deditius et al., 2011; Hough et al., 2011; Mikhlin et al., 2011; Reich et al., 2005; Reich and Becker, 2006). While the presence of As in pyrite has probably aided in the adsorption and accumulation of Au in pyrite in the Derwent samples As is not significantly enriched in the sections where

414 strong Au enrichment is observed. Thus, relative As enrichment in pyrite probably did not
415 result in relative enrichment of Au in pyrite.

416 Inclusions were found to be an important host of the Ag in diagenetic pyrite. This is
417 consistent with several other studies that have found silver to form Ag metal or Ag sulfide
418 micro particles on or in pyrite (Deditius et al., 2011; Mikhlin et al., 2011; Müller et al., 2002;
419 Pooley and Shrestha, 1996). Previous studies have suggested that these form first as films of
420 Ag_2S that can consolidate into round nanoparticles. Over time these sulphides can
421 decompose to Ag metal (Mikhlin et al., 2011). Similarly to Au, the Ag in pyrite is at a
422 maximum below the major zone of metal contamination (Figure 4). The pK_1 for the $MeOH^{z-}$
423 ^{1} of Ag is 12 (Baes and Mesmer, 1976), which suggests that the pH conditions of the
424 sediments are not as ideal for Ag adsorption on pyrite as for some other elements (notably
425 Cu, Pb and Zn) (Müller et al., 2002). This coupled with a far greater amount of competition
426 for binding sites with Cu, Pb and Zn higher in the section resulted in relatively low Ag in
427 pyrite in the more metal enriched part of the sediment and high Ag in pyrite below the major
428 metal enrichment. This is similar to explanations given for low Ag adsorption in zones of
429 high Pb, Cu and Zn adsorption for studies of mine tailings (Müller et al., 2002).

430 The Ni content of pyrite is generally subdued in most of the Derwent pyrite, despite Ni
431 commonly being enriched in pyrite. This is due to the general low levels of Ni in the system.
432 The amount of Co in pyrite is similarly subdued, though not to the extent of Ni and probably
433 stems from a similar lack of Co available for adsorption (Figure 6). Competition for
434 adsorption sites on the pyrite may also play a role in the low levels of Ni and Co in the metal
435 enriched sections. This would explain why the highest average Ni and Co enrichment is
436 found in pyrite from the 70 to 75 cm section, coincident with the highest Ag in pyrite. This
437 again is consistent with the explanation for lower adsorption of less abundant trace metals on
438 pyrite when there is significant competition for adsorption sites by Müller et al. (2002).

439 The reason for the high Te measured within the Derwent pyrite framboids compared to the
440 Huon framboids is not immediately clear, particularly as the total amount of Te (whole
441 sediment) are similar. It may be due to complexing between tellurium and other elements
442 (such as gold) in solution, causing the tellurium to be adsorbed onto the pyrite with the other
443 metals or that Te in the Huon is hosted in an insoluble detrital mineral and is not available for
444 incorporation into pyrite.

445 As there is no data for the amount of mobile Au, Ag and Te available in the sediments at
446 different depths due to analytical difficulties with measuring these elements in the sequential
447 leaches, we cannot be certain of our competition for adsorption site hypothesis for siting of
448 these elements in diagenetic pyrite. Other explanations for the observations may be that the
449 Au, Ag and Te are entirely held within immobile phases such as franklinite or sulphides in
450 the more contaminated zones and held within more soluble phases, such as organic matter
451 immediately below the contaminated zone. We see this explanation as unlikely because the
452 source of the Au, Ag and Te appears to be the smelter waste and for it to diffuse down to
453 enter the pyrite below the contamination it would have to be mobile and thus would be
454 available for incorporation into the pyrite earlier as well. A second possibility is that trace
455 metal incorporation is at least to some degree controlled by biological processes and the
456 organisms that are needed cannot live in the high metal conditions of the higher sections of
457 the core. Though this is an interesting possibility it is well out of our field of expertise and
458 we are unable to test it at this time.

459 This is the first study that has analysed pyrite framboids that have formed in a contaminated
460 estuary. It shows the amount of trace elements that can be incorporated into pyrite and thus
461 be rendered unavailable for biological uptake. The study also shows how the incorporation
462 of some more concentrated trace elements can limit the incorporation of other trace elements.

463 The use of LA-ICPMS has allowed the analysis gold, silver and tellurium in sedimentary
464 pyrite, something not possible using traditional sequential extraction techniques. This
465 demonstrates some of the factors that affect the uptake of these elements in sedimentary
466 pyrite which is of particular interest now as recent models for ore deposits suggest pyrite is an
467 important source for some metals and metalloids.

468

469 **ACKNOWLEDGEMENTS**

470 The authors thank Viola Services and Mark Stalker for donation of time and equipment
471 during the sampling of the Derwent sediments and John Gibson and Kerrie Swadling for use
472 of the hammer corer. Thanks also to Sandrin Feig and Karsten Goemann for their aid in the
473 SEM analyses and aiding in composition of the methods section and to Leonid Danyushevsky
474 and Sarah Gilbert for their expert advice in the use of LA-ICPMS and for aiding in the
475 composition of the methods section. Thanks also to Lee Groat, Jacqueline Halpin and Selina
476 Wu for invaluable comments on early drafts of the manuscript and Kate Bromfield for help
477 with mineral separations. Michael Roach's help with collection of the Huon cores was greatly
478 appreciated. Thank you also to Martin Reich and Zsolt A. Berner whose insightful comments
479 greatly increased the quality of this manuscript.

480 REFERENCES
481
482 Algeo, T.J. (2004) Can marine anoxic events draw down the trace element inventory of
483 seawater? Geology, 32, 1057-1060.
484 Anbar, A.D., Duan, Y., Lyons, T.W., Arnold, G.L., Kendall, B., Creaser, R.A., Kaufman,
485 A.J., Gordon, G.W., Scott, C., and Garvin, J. (2007) A whiff of oxygen before the
486 great oxidation event? Science, 317, 1903-1906.
487 Baes, C. F., and Mesmer, R. E., 1976, The hydrolysis of cations, Wiley New York.
488 Berner, Z., Pujol, F., Neumann, T., Kramar, U., Stüben, D., Racki, G., and Simon, R. (2006),
489 Contrasting trace element composition of diagenetic and syngenetic pyrites:
490 implications for the depositional environment, *in* Proceedings Geophysical Research
491 Abstracts 8, 8281.

Berner, Z. A., Puchelt, H., NÖLtner, T., and Kramar, U. T. Z. (2013) Pyrite geochemistry in the Toarcian Posidonia Shale of south-west Germany: Evidence for contrasting trace-element patterns of diagenetic and syngenetic pyrites: Sedimentology, 60, 548-573.

Borah, D., and Senapati, K. (2006) Adsorption of Cd(II) from aqueous solution onto pyrite: Fuel, 85, 1929-1934.

Danyushevsky, L., Robinson, P., Gilbert, S., Norman, M., Large, R., McGoldrick, P., and Shelley, M. (2011) Routine quantitative multi-element analysis of sulphide minerals by laser ablation ICP-MS: Standard development and consideration of matrix effects. Geochemistry: Exploration, Environment, Analysis, 11, 51-60.

Deditius, A. P., Utsunomiya, S., Ewing, R. C., and Kesler, S. E. (2009) Nanoscale "liquid" inclusions of As-Fe-S in arsenian pyrite: American Mineralogist, 94, 391-394.

Deditius, A. P., Utsunomiya, S., Reich, M., Kesler, S. E., Ewing, R. C., Hough, R., and Walshe, J. (2011) Trace metal nanoparticles in pyrite: Ore Geology Reviews, 42, 32-46.

Deditius, A. P., Utsunomiya, S., Renock, D., Ewing, R. C., Ramana, C. V., Becker, U., and Kesler, S. E. (2008) A proposed new type of arsenian pyrite: Composition, nanostructure and geological significance: Geochimica et Cosmochimica Acta, 72,2919-2933.

Dellwig, O., Böttcher, M. E., Lipinski, M., and Brumsack, H.-J. (2002) Trace metals in Holocene coastal peats and their relation to pyrite formation (NW Germany): Chemical Geology, 182, 423-442.

Donald, R., and Southam, G. (1999) Low temperature anaerobic bacterial diagenesis of ferrous monosulfide to pyrite. Geochimica et Cosmochimica Acta, 63, 2019-2023.

Erickson, B. E., and Helz, G. R. (2000) Molybdenum (VI) speciation in sulfidic waters:: Stability and lability of thiomolybdates: Geochimica et Cosmochimica Acta, 64, 1149-1158.

Gregory, D., Meffre, S., and Large, R. (2013) Mineralogy of metal contaminated estuarine sediments, Derwent estuary, Hobart, Australia: implications for metal mobility: Australian Journal of Earth Sciences, 60, p. 589-603.

Guillong M, Meier D, Allan M, Heinrich C, Yardley (2008) 'SILLS: a Matlab-based program for the reduction of laser ablation ICP-MS data of homogeneous materials and inclusions', in: 'Laser Ablation ICP-MS in the earth sciences: Current practices and outstanding issues', Paul Sylvester (Ed.), Mineral Association of Canada Short Course Series 40, Vancouver, Canada

Gwynne, P. (2013) Microbiology: There's gold in them there bugs: Nature, 495, S12-S13.

Helz, G., Miller, C., Charnock, J., Mosselmans, J., Pattrick, R., Garner, C., and Vaughan, D. (1996) Mechanism of molybdenum removal from the sea and its concentration in black shales: EXAFS evidence: Geochimica et Cosmochimica Acta, 60, 3631-3642.

Hochella, M.F., Kasama, T., Putnis, A., Putnis, C.V., and Moore, J.N. (2005) Environmentally important, poorly crystalline Fe/Mn hydrous oxides: Ferrihydrite and a possibly new vernadite-like mineral from the Clark Fork River Superfund Complex. American Mineralogist, 90, 718-724.

Hough, R. M., Noble, R. R. P., and Reich, M. (2011) Natural gold nanoparticles: Ore Geology Reviews, 42, 55-61.

Huerta-Diaz, M.A., and Morse, J.W. (1990) A quantitative method for determination of trace metal concentrations in sedimentary pyrite. Marine Chemistry, 29, 119-144.

Huerta-Diaz, M.A., and Morse, J.W. (1992) Pyritization of trace metals in anoxic marine sediments. Geochimica et Cosmochimica Acta, 56, 2681-2702.

Jean, G.E., and G Michael, B. (1985) An XPS and SEM study of gold deposition at low temperatures on sulphide mineral surfaces: Concentration of gold by adsorption/reduction. Geochimica et Cosmochimica Acta, 49, 979-987.

Jean, G. E., and Bancroft, G. M. (1986) Heavy metal adsorption by sulphide mineral surfaces: Geochimica et Cosmochimica Acta, 50, 1455-1463.

Jones, B., Chenhall, B., Debretsion, F., and Hutton, A. (2003) Geochemical comparisons between estuaries with non-industrialised and industrialised catchments: the Huon and Derwent River estuaries, Tasmania. Australian Journal of Earth Sciences, 50, 653-667.

Konhauser, K.O. (1998) Diversity of bacterial iron mineralization. Earth-Science Reviews, 43, 91-121.

Large, R.R., Danyushevsky, L., Hollit, C., Maslennikov, V., Meffre, S., Gilbert, S., Bull, S., Scott, R., Emsbo, P., Thomas, H., Singh, B., and Foster, J. (2009) Gold and Trace Element Zonation in Pyrite Using a Laser Imaging Technique: Implications for the Timing of Gold in Orogenic and Carlin-Style Sediment-Hosted Deposits. Economic Geology, 104, 635-668.

Large, R.R., Maslennikov, V.V., Robert, F., Danyushevsky, L.V., and Chang, Z.S. (2007) Multistage sedimentary and metamorphic origin of pyrite and gold in the giant Sukhoi Log deposit, Lena gold province, Russia. Economic Geology, 102, 1233-1267.

Lengke, M.F., Fleet, M.E., and Southam, G. (2006) Morphology of gold nanoparticles synthesized by filamentous cyanobacteria from gold (I)-thiosulfate and gold (III)-chloride complexes. Langmuir, 22, 2780-2787.

Lennie, A.R., England, K.E., and Vaughan, D.J. (1995) Transformation of synthetic mackinawite to hexagonal pyrrhotite: A kinetic study. American Mineralogist, 80, 960-967.

Longerich, H.P., Jackson, S.E., and Günther, D. (1996) Inter-laboratory note. Laser ablation inductively coupled plasma mass spectrometric transient signal data acquisition and analyte concentration calculation. Journal of Analytical Atomic Spectrometry, 11, 899-904.

Lord, C.J.I. (1982) A Selective and Precise Method for Pyrite Determination in Sedimentary Materials: Research-Method Paper. Journal of Sedimentary Research, 52.

Lowers, H.A., Breit, G.N., Foster, A.L., Whitney, J., Yount, J., Uddin, M.N., and Muneem, A.A. (2007) Arsenic incorporation into authigenic pyrite, Bengal Basin sediment, Bangladesh. Geochimica et Cosmochimica Acta, 71, 2699-2717.

Maddox, L.M., Bancroft, G.M., Scaini, M., and Lorimer, J. (1998) Invisible gold; comparison of Au deposition on pyrite and arsenopyrite. American Mineralogist, 83, 1240-1245.

Martin, J., Nirel, P., and Thomas, A. (1987) Sequential extraction techniques: promises and problems. Marine Chemistry, 22, 313-341.

Mikhlin, Y., Romanchenko, A., Likhatski, M., Karacharov, A., Erenburg, S., and Trubina, S., (2011) Understanding the initial stages of precious metals precipitation: Nanoscale metallic and sulfidic species of gold and silver on pyrite surfaces: Ore Geology Reviews, 42, 47-54.

Milne, T. (2012) 2010/2011 report for Nyrstar Hobart pty. ltd., Nyrstar Hobart Smelter – Lutana, TAS, accessed 10 April, 2013, <http://www.npi.gov.au/npidata/action/load/emission-by-individual-facility-result/criteria/state/TAS/year/2011/jurisdiction-facility/TAS%20120.

Morse, J., and Luther, G. (1999) Chemical influences on trace metal-sulfide interactions in anoxic sediments. Geochimica et Cosmochimica Acta, 63, 3373-3378.

Morse, J.W., and Arakaki, T. (1993) Adsorption and coprecipitation of divalent metals with mackinawite (FeS). Geochimica et Cosmochimica Acta, 57, 3635-3640.

Müller, B., Axelsson, M. D., and Öhlander, B. (2002) Adsorption of trace elements on pyrite surfaces in sulfidic mine tailings from Kristineberg (Sweden) a few years after remediation: Science of the Total Environment, 298, 1-16.

Mycroft, J., Bancroft, G., McIntyre, N., and Lorimer, J. (1995) Spontaneous deposition of gold on pyrite from solutions containing Au (III) and Au (I) chlorides. Part I: A surface study. Geochimica et Cosmochimica Acta, 59, 3351-3365.

Neumann, T., Rausch, N., Leipe, T., Dellwig, O., Berner, Z., and Böttcher, M. E. (2005) Intense pyrite formation under low-sulfate conditions in the Achterwasser lagoon, SW Baltic Sea: Geochimica et Cosmochimica Acta, 69, 3619-3630.

Neumann, T., Scholz, F., Kramar, U., Ostermaier, M., Rausch, N., and Berner, Z. (2013) Arsenic in framboidal pyrite from recent sediments of a shallow water lagoon of the Baltic Sea: Sedimentology, 60, 1389-1404.

Pikaray, S., Banerjee, S., and Mukherji, S., 2005, Sorption of arsenic onto Vindhyan shales: Role of pyrite and organic carbon: Current Science, v. 88, no. 10, p. 1580-1585.

Pooley, F., and Shrestha, G. (1996) The distribution and influence of silver in pyrite bacterial leaching systems: Minerals engineering, 9, 825-836.

Qian, G., Brugger, J., Testemale, D., Skinner, W., and Pring, A. (2013) Formation of As(II)-pyrite during experimental replacement of magnetite under hydrothermal conditions: Geochimica et Cosmochimica Acta, 100, 1-10.

Reich, M., and Becker, U. (2006) First-principles calculations of the thermodynamic mixing properties of arsenic incorporation into pyrite and marcasite: Chemical Geology, 225, 278-290.

Reich, M., Kesler, S. E., Utsunomiya, S., Palenik, C. S., Chryssoulis, S. L., and Ewing, R. C. (2005) Solubility of gold in arsenian pyrite: Geochimica et Cosmochimica Acta, 69, 2781-2796.

Reith, F., Etschmann, B., Grosse, C., Moors, H., Benotmane, M. A., Monsieurs, P., Grass, G., Doonan, C., Vogt, S., and Lai, B. (2009) Mechanisms of gold biomineralization in the bacterium Cupriavidus metallidurans: Proceedings of the National Academy of Sciences, 106, 17757-17762.

Reith, F., Rogers, S. L., McPhail, D., and Webb, D. (2006) Biomineralization of gold: biofilms on bacterioform gold: Science, 313, 233-236.

Renders, P., and Seward, T. (1989) The adsorption of thio gold (I) complexes by amorphous As_2S_3 and Sb_2S_3 at 25 and 90° C. Geochimica et Cosmochimica Acta, 53, 255-267.

Renock, D., Gallegos, T., Utsunomiya, S., Hayes, K., Ewing, R. C., and Becker, U. (2009) Chemical and structural characterization of As immobilization by nanoparticles of mackinawite (FeS_m): Chemical Geology, 268, 116-125.

Rickard, D., and Luther, G.W. (1997) Kinetics of pyrite formation by the H2S oxidation of iron (II) monosulfide in aqueous solutions between 25 and 125° C: The mechanism. Geochimica et Cosmochimica Acta, 61, 135-147.

Rickard, D., Grimes, S., Butler, I., Oldroyd, A., and Davies, K. L. (2007) Botanical constraints on pyrite formation: Chemical Geology, 236, 228-246.

Rickard, D., and Luther, G. W. (2007) Chemistry of Iron Sulfides: Chemical Reviews, 107, 514-562.

Rosso, K. M., and Vaughan, D. J. (2006) Reactivity of sulfide mineral surfaces: Reviews in Mineralogy and Geochemistry, 61, 557-607.

Schoonen, M., and Barnes, H. (1991) Reactions forming pyrite and marcasite from solution: II. Via FeS precursors below 100 C. Geochimica et Cosmochimica Acta, 55, 1505-1514.

Schoonen, M.A. (2004) Mechanisms of sedimentary pyrite formation. Special Papers-Geological Society of Amaerica, 117-134.

Schoonen, M.A., Fisher, N.S., and Wente, M. (1992) Gold sorption onto pyrite and goethite: A radiotracer study. Geochimica et cosmochimica Acta, 56, 1801-1814.

Thomas, H.V., Large, R.R., Bull, S.W., Maslennikov, V., Berry, R.F., Fraser, R., Froud, S., and Moye, R. (2011) Pyrite and pyrrhotite textures and composition in sediments, laminated quartz veins, and reefs at Bendigo gold mine, Australia: insights for ore genesis. Economic Geology, 106, 1-31.

Tribovillard, N., Algeo, T.J., Lyons, T., and Riboulleau, A. (2006) Trace metals as paleoredox and paleoproductivity proxies: An update. Chemical Geology, 232, 12-32.

Wang, X., Forssberg, K., and Bolin, N. (1989) Adsorption of copper (II) by pyrite in acidic to neutral pH media: Scandinavian Journal of Metallurgy, 18, 262-270.

Whitehead, J., Coughanowr, C., Agius, J., Chrispijn, J., Taylor, U., and Wells, F. (2010) State of the Derwent Estuary 2009: a review of pollution sources, loads and environmental quality data from 2003 – 2009. Derwent Estuary Program, DPIPWE, Tasmania.

Widler, A., and Seward, T. (2002) The adsorption of gold (I) hydrosulphide complexes by iron sulphide surfaces. Geochimica et Cosmochimica Acta, 66, 383-402.

Wolthers, M., Van der Gaast, S.J., and Rickard, D. (2003) The structure of disordered mackinawite. American Mineralogist, 88, 2007-2015.

Woods, R. (1996) Chemisorption of Thiols on Metals and Metal Sulfide. Modern Aspects of Electrochemistry, 29, 401-453.

Xu, N., Christodoulatos, C., and Braida, W. (2006) Adsorption of molybdate and tetrathiomolybdate onto pyrite and goethite: Effect of pH and competitive anions: Chemosphere, 62, 1726-1735.

Xia, F., Brugger, J., Chen, G., Ngothai, Y., O'Neill, B., Putnis, A., and Pring, A. (2009) Mechanism and kinetics of pseudomorphic mineral replacement reactions: a case study of the replacement of pentlandite by violarite. Geochimica et Cosmochimica Acta, 73, 1945-1969.

Zeien, H., and Brümmer, G. W., 1989, (in German) Chemische Extraktion zur Bestimmung von Schwermetallbindungsformen in Böden: Mitteilungen der Deutschen Bodenkundlichen Gesellschaft, 59, 505-510.

Zhang, J., Lu, J., Zhai, J., and Yang, F., 1997, Simulating experiments on enrichment of gold by bacteria and their geochemical significance: Chinese Journal of Geochemistry, 16, 369-373.

Figure Captions

Figure 1: Location of samples taken from the Derwent (SM1001) and Huon (H1) Estuaries. Hatched patterns indicate residential areas.

Figure 2: Scanning electron microscope images of pyrite framboids from the Derwent Estuary (A and B) and the Huon Estuary (C to F). The framboids are very similar between the relatively uncontaminated Huon Estuary and the contaminated Derwent Estuary.

Figure 3: Whole sediment geochemical analyses of sediment cores from the Derwent (red) and Huon (blue) Estuaries. The Derwent estuary is enriched in metals and metalloids in the top 45 cm, very enriched from 45-55 cm and tapers down to background values by 75 cm.

Figure 4: Whole sediment analyses (red squares) and LA-ICPMS analyses (blue circles) of pyrite framboids from the Derwent (left) and Huon (right) Estuaries.

Figure 5: Time resolved LA-ICPMS output graphs of pyrite framboid analyses for Derwent and Huon Estuaries. The trace of the iron (when above 1000000 counts) shows where pyrite is being ablated. Spikes in the plots show microinclusions within the pyrite while relatively flat plots indicated the elements are held within the pyrite structure. The framboids are mounted in epoxy then polished down resulting in the laser starting in the center and ablating to the edge.

Figure 6: Trace metal contents of pyrite, whole sediment and trace metals available to be incorporated into pyrite. Note that both Pb and Zn have very high proportions of metals that can be incorporated into pyrite. This may cause some metals to be unable to adsorb onto the surface of the growing pyrite allowing them to diffuse to lower levels in the sediment and become incorporated into the pyrite there.

Tables

Table 1: Trace metals that are easily exchanged, weakly complexed and bound by carbonates, bound by Mn (hydr)oxides and bound by organic matter from the Derwent Estuary sediments as determined by Gregory et al. (2013).

Depth Interval (cm)	Lead (ppm)	Manganese (ppm)	Cobalt (ppm)	Nickel (ppm)	Copper (ppm)	Zinc (ppm)	Arsenic (ppm)	Cadmium (ppm)	Molybdenum (ppm)
20-25	1415	51.5	3.0	4.0	143	1935	33.8	17.8	0.56
30-35	2007	87.5	4.1	9.7	225	3459	130.1	21.1	1.22

50-55	4750	276.6	5.4	2.8	172	4645	165.7	16.4	0.59
90-95	9.392	24.8	1.3	4.1	7.5	11.7	0.44	0.62	0.15

*Specific values for the different extraction step and error estimates can be found in Gregory et al., (2013).

Table 2 Maximum, Minimum and Median LA-ICPMS analyses of pyrite from the Derwent Estuary

Zn			Pb (ppm)			Cu (ppm)			Bi (ppm)			Ni (ppm)			Co (ppm)		
Max	Med	Min	Max	Med	Min	Max	Med	Min	Max	Med	Min	Max	Med	Min	Max	Med	Min	Max
4370	1400	1320	10600	460	206	704	2.95	1.44	11.23	15.04	1.64	31.7	23.5	4.59	81.3			
708	54.5	1.2	1620	17.9	7.55	451	<0.13	<0.09	2.05	2.04	0.79	8.9	18.9	3.06	57.0			
9410	1250	66.8	7290	154	28.2	640	0.36	<0.15	2.38	1.35	<0.56	6.7	12.7	2.09	112			
4540	808	4.9	6130	77.2	16.9	704	0.24	<0.12	4.55	2.84	1.20	80.1	11.7	3.28	146			
2500	635	19.3	3010	102	6.81	273	0.30	<0.06	2.06	0.85	<0.62	5.3	8.9	0.63	56.6			
2460	237	4.3	4970	44.8	2.37	670	0.19	<0.09	2.53	3.61	<0.46	150	9.6	<0.15	667			
1230	211	7.3	1140	130	18.7	351	0.13	<0.04	0.49	6.11	2.77	9.6	32.2	11.9	81.6			
899	184	24.0	1290	79.1	12.0	157	0.09	<0.03	0.25	35.0	5.58	84.2	83.9	2.31	212			
111	55.7	1.4	128	25.2	4.93	56	0.07	<0.03	0.23	4.58	1.22	15.5	2.2	0.29	20.0			
114	29.9	5.9	46	35.0	14.8	209	0.05	<0.02	0.24	9.92	2.20	33.3	1.6	0.72	35.5			
Mo			As (ppm)			Au (ppm)			Ag (ppm)			Te (ppm)						
Max	Med	Min	Max	Med	Min	Max	Med	Min	Max	Med	Min	Max						
3.4	600	258	2300	0.31	<0.21	0.80	2.90	2.54	3.25	<2.88	<2.54	2.88						
3.7	1730	264	6210	<0.07	<0.03	0.07	<0.17	<0.11	3.32	0.78	0.09	1.17						
				0.04	<0.19	0.19				1.35	<0.62	2.66						
14.2	3140	685	4480	0.10	<0.57	0.57	0.82	<0.17	1.60	4.33	0.88	7.07						
50.3	758	9	4080	0.03	<1.01	5.98	1.16	<1.15	3.62	2.05	0.59	11.8						
32.4	587	193	2520	0.05	<0.49	0.49	0.23	<0.10	1.93	2.16	0.22	12.4						
120	795	106	5420	0.08	<0.10	0.45	0.37	<0.24	7.64	3.38	0.58	12.0						
5.4	1120	680	2020	0.81	<0.16	3.52	4.32	0.58	8.66	1.01	<1.31	6.78						
73.3	1720	18	6990	0.35	<0.18	0.87	24.0	0.20	90.2	2.49	<1.65	9.60						
13.6	703	200	1140	0.04	<0.16	0.21	0.63	0.05	26.5	1.51	<1.67	4.39						
11.0	125	61	624	0.30	<0.14	0.70	0.26	<0.41	38.1	1.72	<1.83	3.75						

Depth																																			
(cm)	Med	Min																																		
5 - 10	591	453																																	
15 -20	84	24																																	
20 - 25																																			
25 - 30	1180	106																																	
35 - 40	723	92																																	
40 - 45	298	192																																	
50 - 55	515	34																																	
60 - 65	415	287																																	
70 - 75	326	229																																	
80 - 85	82	45																																	
90 - 95	94	24																																	
	Med	Min																																	
5 - 10	2.83	2.13																																	
15 -20	1.48	0.92																																	
20 - 25																																			
25 - 30	3.84	0.39																																	
35 - 40	1.06	<0.46																																	
40 - 45	0.40	<0.41																																	
50 - 55	1.93	<0.56																																	
60 - 65	2.87	1.33																																	
70 - 75	22.1	3.33																																	
80 - 85	4.35	0.81																																	
90 - 95	3.19	1.41																																	

703

704 Table 3 Maximum, Minimum and Median LA-ICPMS analyses of pyrite from the Huon

705 Estuary

Pb (ppm	Cu (ppm)			Bi (ppm)			Ni (ppm)			Co (ppm)																										
Max	Med	Min	Max	Med	Min	Max	Med	Min	Max	Med	Min	Max																								
27.1	10.7	0.68	45.1	0.07	<0.03	0.38	18.0	0.18	79.6	13.6	<0.05	542																								
10.2	17.2	3.74	169	0.04	<0.03	0.23	2.77	0.53	67.4	2.51	0.14	152																								
6.83	19.3	1.10	223	0.09	<0.03	0.30	2.89	1.95	87.5	3.59	0.49	153																								
26.4	30.9	0.75	212	0.05	<0.02	0.33	9.12	0.39	70.0	6.74	0.08	133																								
18.1	68.0	20.5	510	0.05	<0.02	0.33	3.96	1.07	34.8	0.87	0.15	109																								
49.1	82.0	3.78	1300	0.12	<0.04	1.11	18.8	2.99	132	25.7	0.74	568																								
As (ppm	Au (ppm)			Ag (ppm)			Te (ppm)																													
Max	Med	Min	Max	Med	Min	Max	Med	Min	Max																											
525	<0.02	<0.01	<0.04	<0.04	<0.03	0.17	0.26	<0.16	0.95																											
3450	<0.03	<0.02	0.09	0.07	<0.04	0.62	<0.31	<0.22	0.39																											
1110	<0.03	<0.02	0.05	<0.05	<0.04	0.13	<0.28	<0.20	1.53																											
1920	<0.03	<0.01	<0.05	<0.06	<0.03	0.41	<0.28	<0.20	2.99																											
2210	<0.03	<0.02	0.04	<0.05	<0.03	0.16	<0.26	<0.21	1.23																											
1650	<0.03	<0.02	0.06	0.05	<0.03	0.49	<0.23	<0.15	1.72																											

Depth (cm)	Zn (ppm)			Mo (ppm)		
	Med	Min	Max	Med	Min	Max
10 - 15	36.6	5.35	272	14.4	0.14	200
20 - 25	25.7	7.60	103	12.0	4.22	20.8
30 - 35	27.1	14.4	67.0	5.32	0.52	246
40 - 45	65.3	5.22	121	14.2	1.37	52.4
50 - 55	59.3	28.4	144	30.2	4.95	202
60 - 65	62.1	13.2	168	40.0	1.32	219
	Med	Min		Med	Min	
	2.00	0.06		181	52.8	
	0.30	0.11		354	91.1	
	2.40	0.07		590	126	
	0.93	0.04		209	46.1	
	1.31	0.13		194	41.0	
	2.53	0.26		122	36.0	

Note: The individual standard deviation of each laser spot varies, however the median values of one standard deviation as calculated by Sills software is as follows: Huon: Ag (0.049), As (5.42), Au (0.026), Cu (4.85), Mo (0.95), Pb (0.33), Te (0.25), Mn (21.98) and Zn (2.24); Derwent: Ag (0.13), As (16.91), Au (0.053), Cu (3.45), Mo (0.31), Pb (4.26), Te (0.26), Mn (21.76) and Zn (6.15).

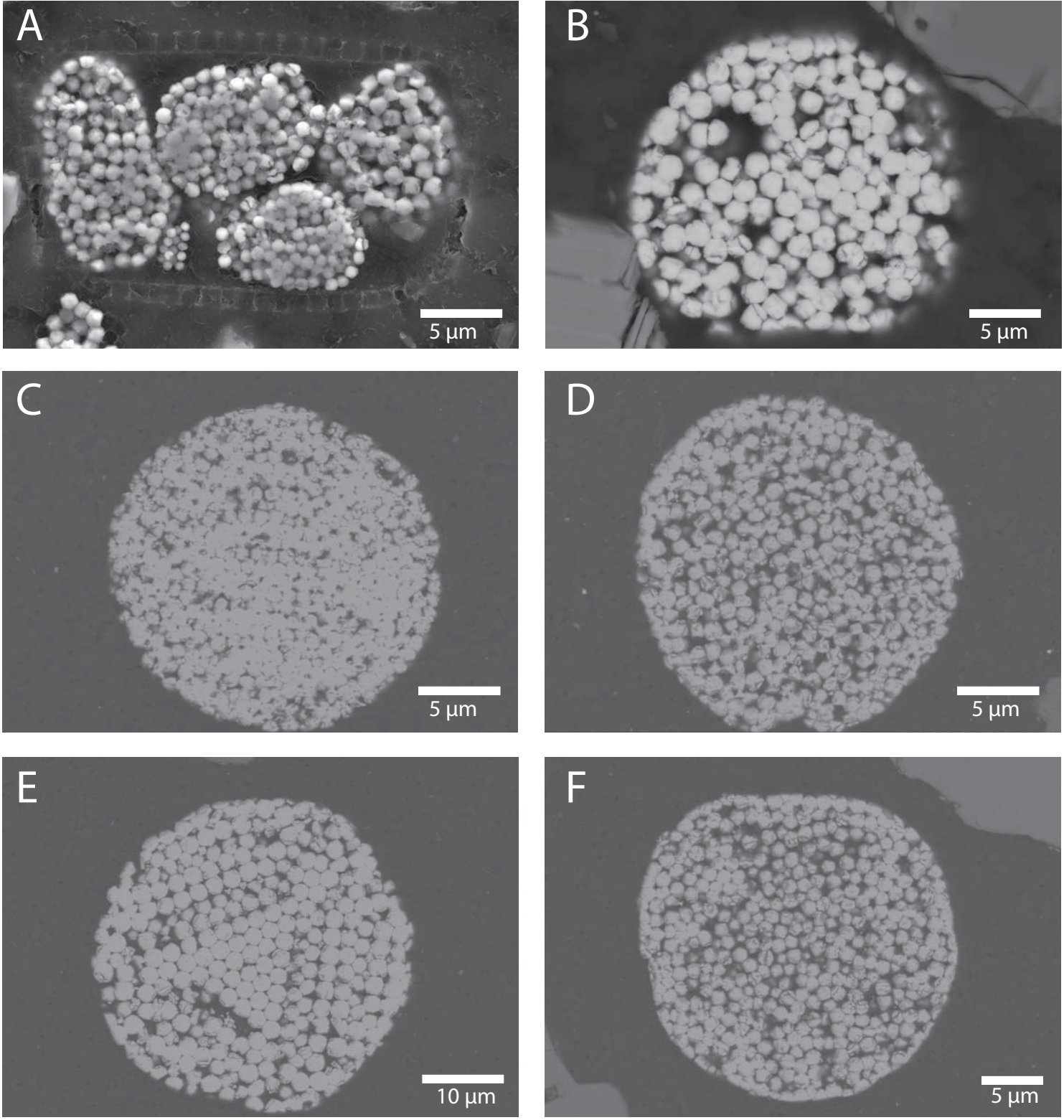
A
5 µm
B
5 µm
C
5 µm
D
5 µm
E
10 µm
F
5 µm

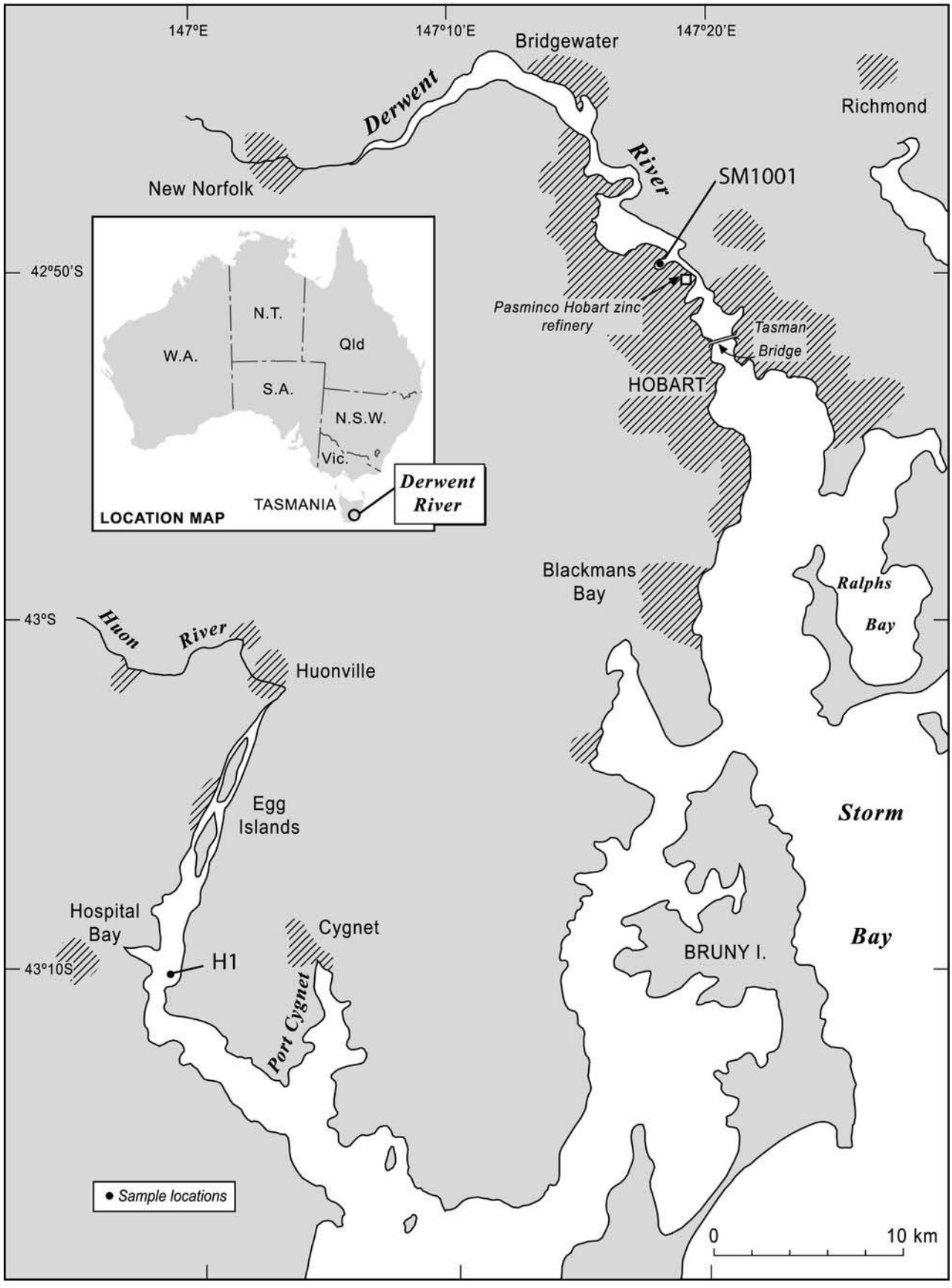
147°E
147°10'E
147°20'E
Bridgewater
Derwent
River
Richmond
New Norfolk
SM1001
42°50'S
Pasminco Hobart zinc refinery
Tasman Bridge
HOBART
N.T.
W.A.
Qld
S.A.
N.S.W.
Vic.
TASMANIA
Derwent River
LOCATION MAP
Blackmans Bay
Ralphs Bay
43°S
Huon River
Huonville
Egg Islands
Storm Bay
Hospital Bay
Cygnet
43°10S
H1
BRUNY I.
Port Cygnet
• Sample locations
0
10 km

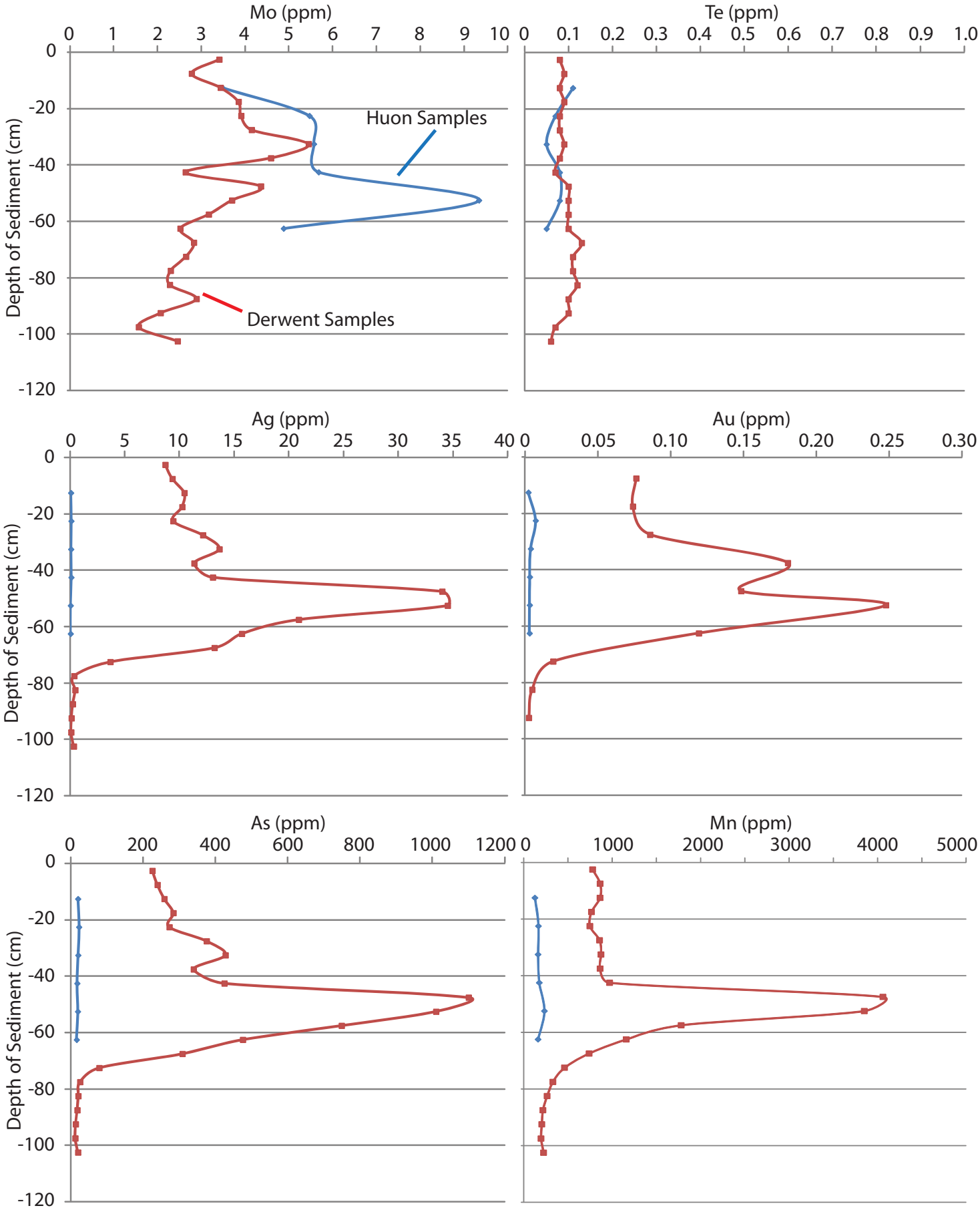
Mo (ppm)
Te (ppm)
Ag (ppm)
Au (ppm)
As (ppm)
Mn (ppm)
Depth of Sediment (cm)
Huon Samples
Derwent Samples

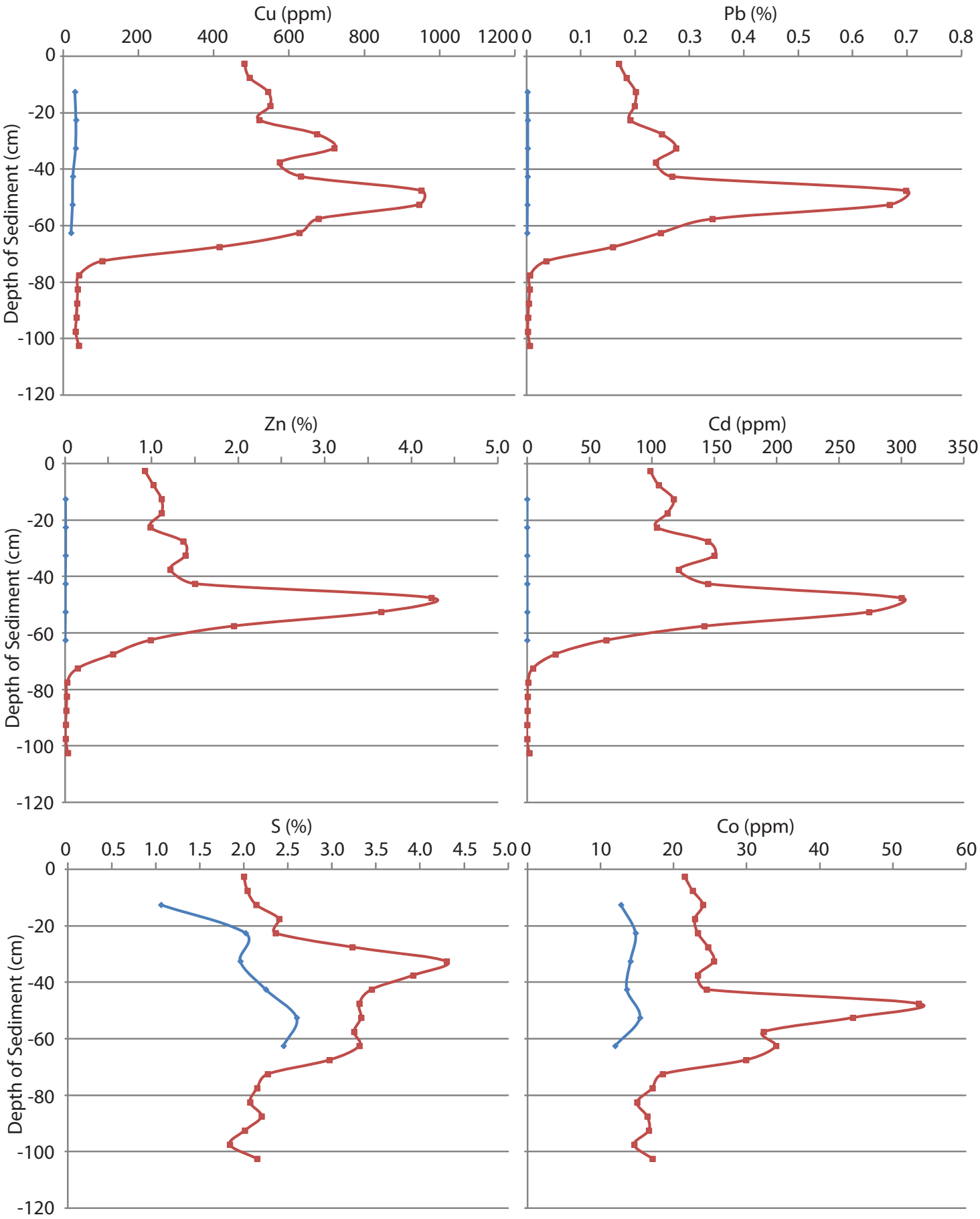
Cu (ppm)
0
200
400
600
800
1000
1200
Pb (%)
0
0.1
0.2
0.3
0.4
0.5
0.6
0.7
0.8
Zn (%)
0
1.0
2.0
3.0
4.0
5.0
Cd (ppm)
0
50
100
150
200
250
300
350
S (%)
0
0.5
1.0
1.5
2.0
2.5
3.0
3.5
4.0
4.5
5.0
Co (ppm)
0
10
20
30
40
50
60
Depth of Sediment (cm)
0
-20
-40
-60
-80
-100
-120

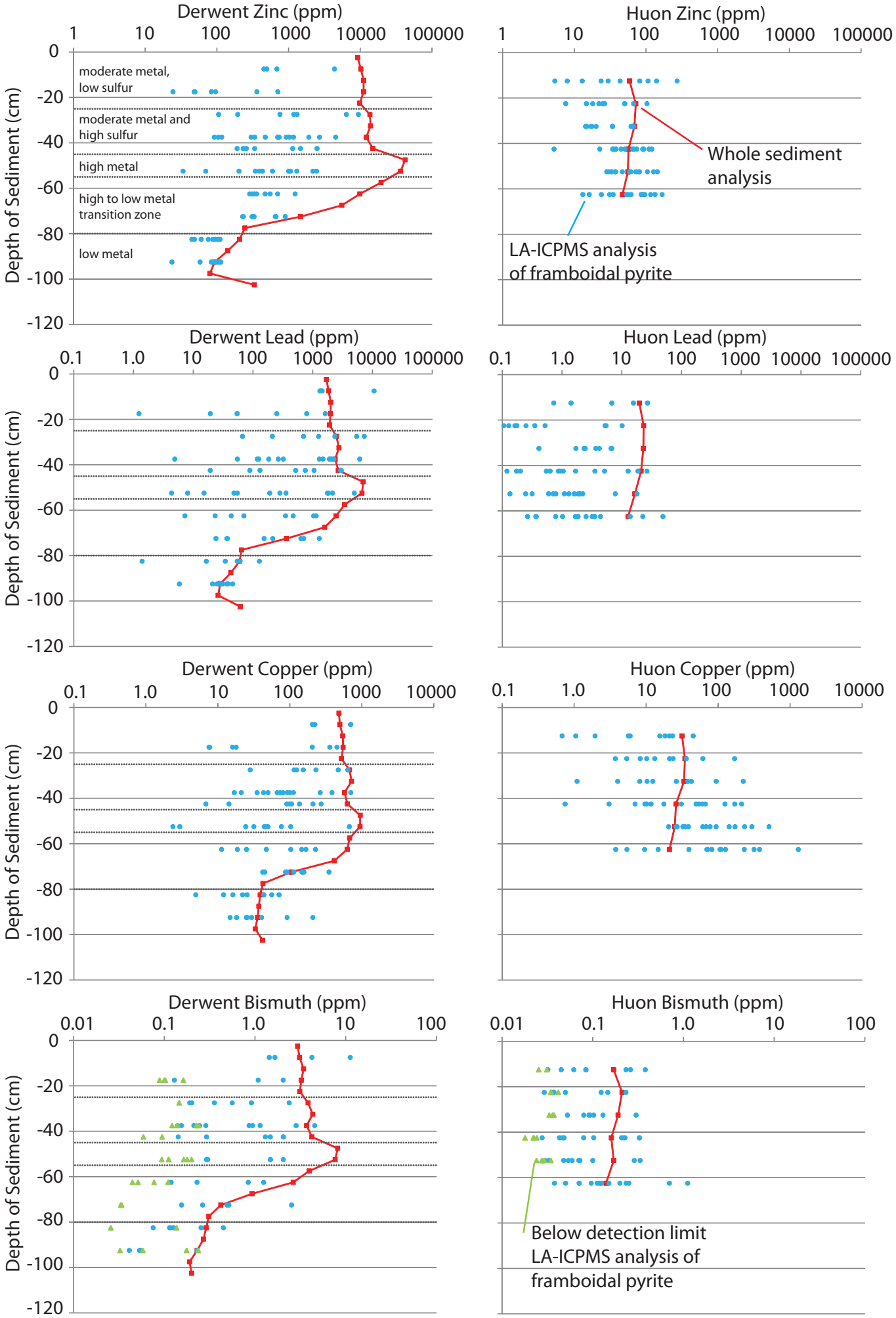
Derwent Zinc (ppm)
1
10
100
1000
10000
100000
Depth of Sediment (cm)
0
-20
-40
-60
-80
-100
-120
moderate metal, low sulfur
moderate metal and high sulfur
high metal
high to low metal transition zone
low metal
Huon Zinc (ppm)
Whole sediment analysis
LA-ICPMS analysis of framboidal pyrite
Derwent Lead (ppm)
0.1
1.0
10
100
1000
10000
100000
Huon Lead (ppm)
Derwent Copper (ppm)
Huon Copper (ppm)
Derwent Bismuth (ppm)
0.01
0.1
1.0
10
100
Huon Bismuth (ppm)
Below detection limit
LA-ICPMS analysis of framboidal pyrite

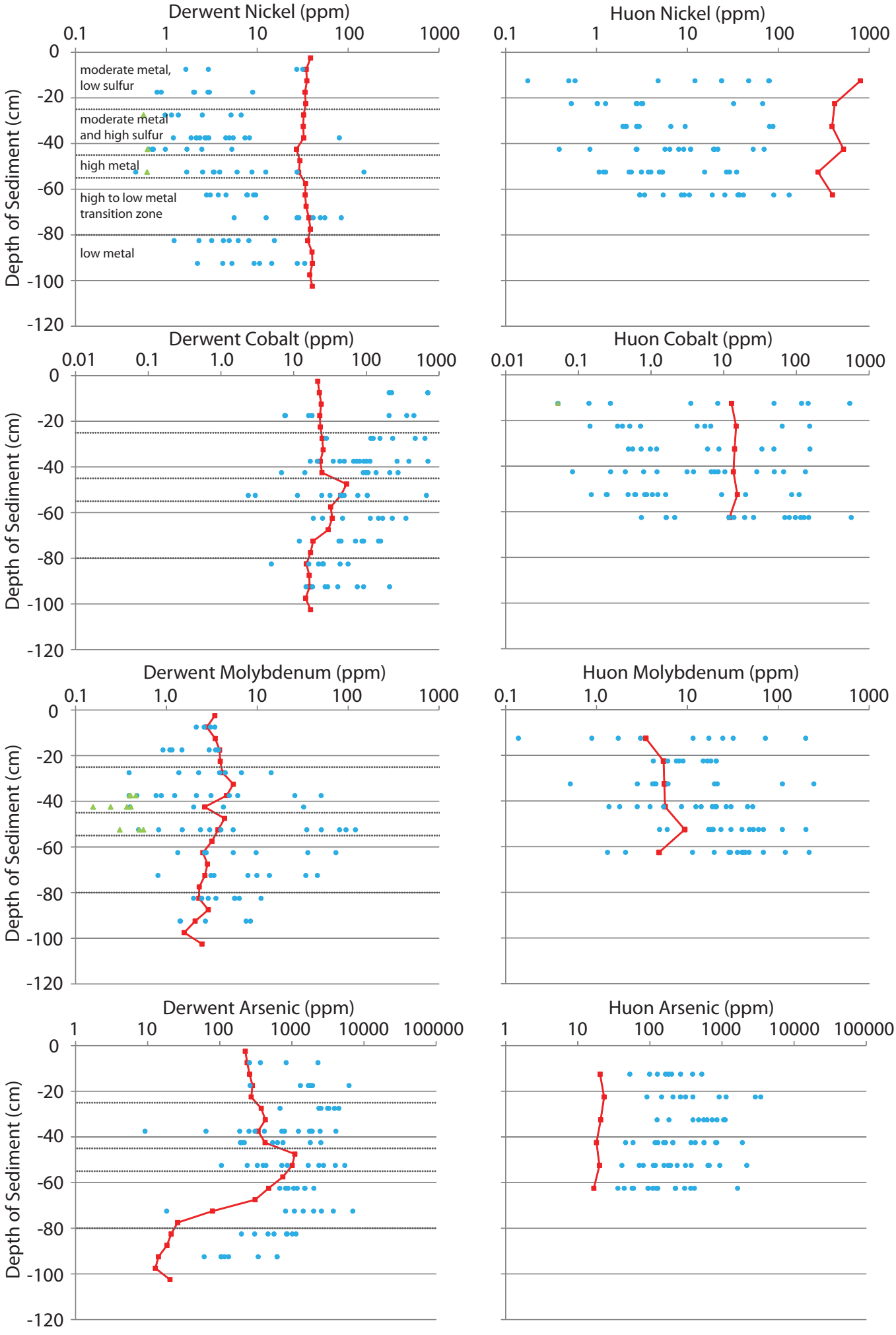
Derwent Nickel (ppm)
Huon Nickel (ppm)
Derwent Cobalt (ppm)
Huon Cobalt (ppm)
Derwent Molybdenum (ppm)
Huon Molybdenum (ppm)
Derwent Arsenic (ppm)
Huon Arsenic (ppm)
Depth of Sediment (cm)
moderate metal, low sulfur
moderate metal and high sulfur
high metal
high to low metal transition zone
low metal

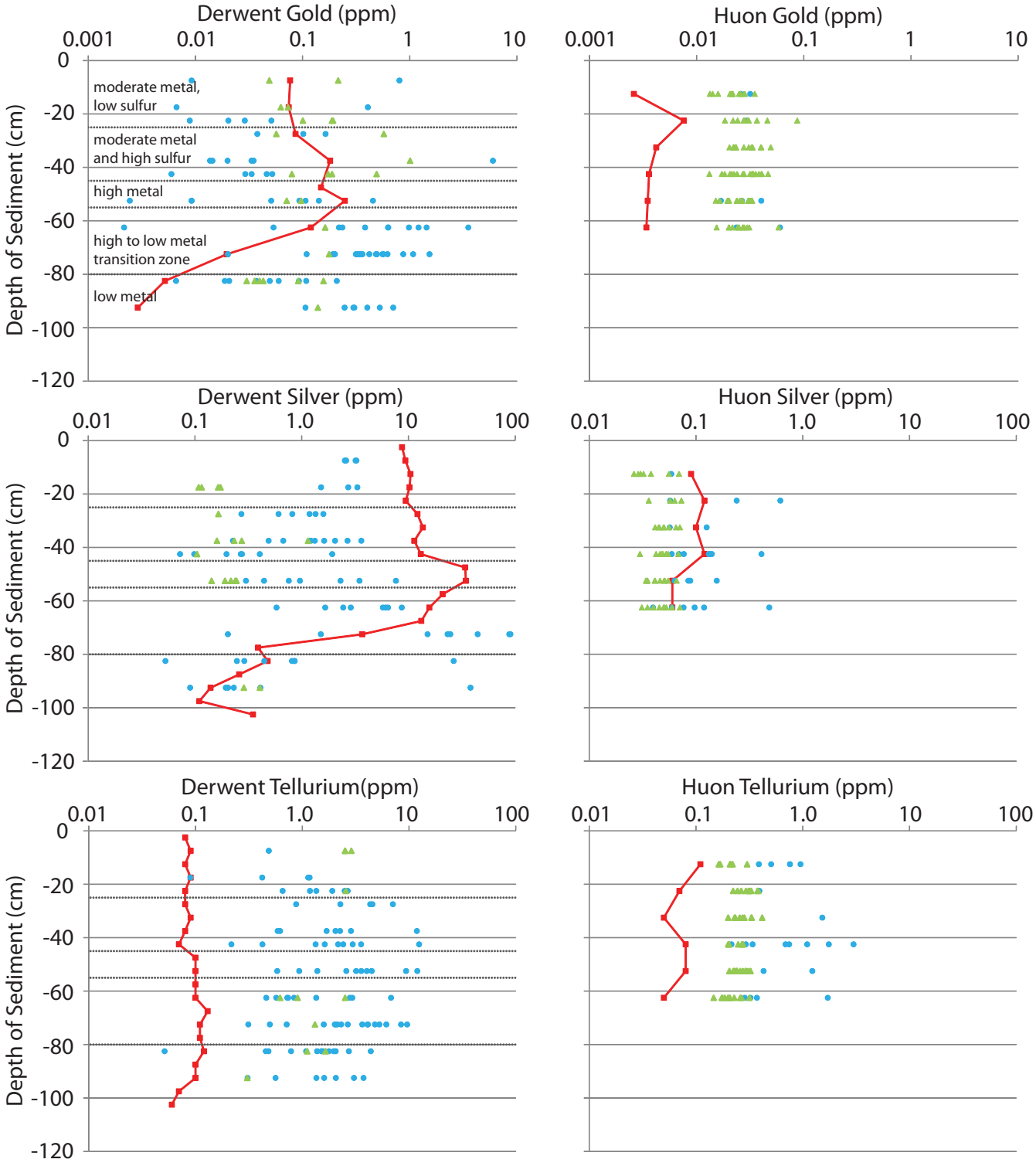
Derwent Gold (ppm)
0.001
0.01
0.1
1
10
Huon Gold (ppm)
Depth of Sediment (cm)
0
-20
-40
-60
-80
-100
-120
moderate metal, low sulfur
moderate metal and high sulfur
high metal
high to low metal transition zone
low metal
Derwent Silver (ppm)
0.01
0.1
1.0
10
100
Huon Silver (ppm)
Derwent Tellurium(ppm)
Huon Tellurium (ppm)

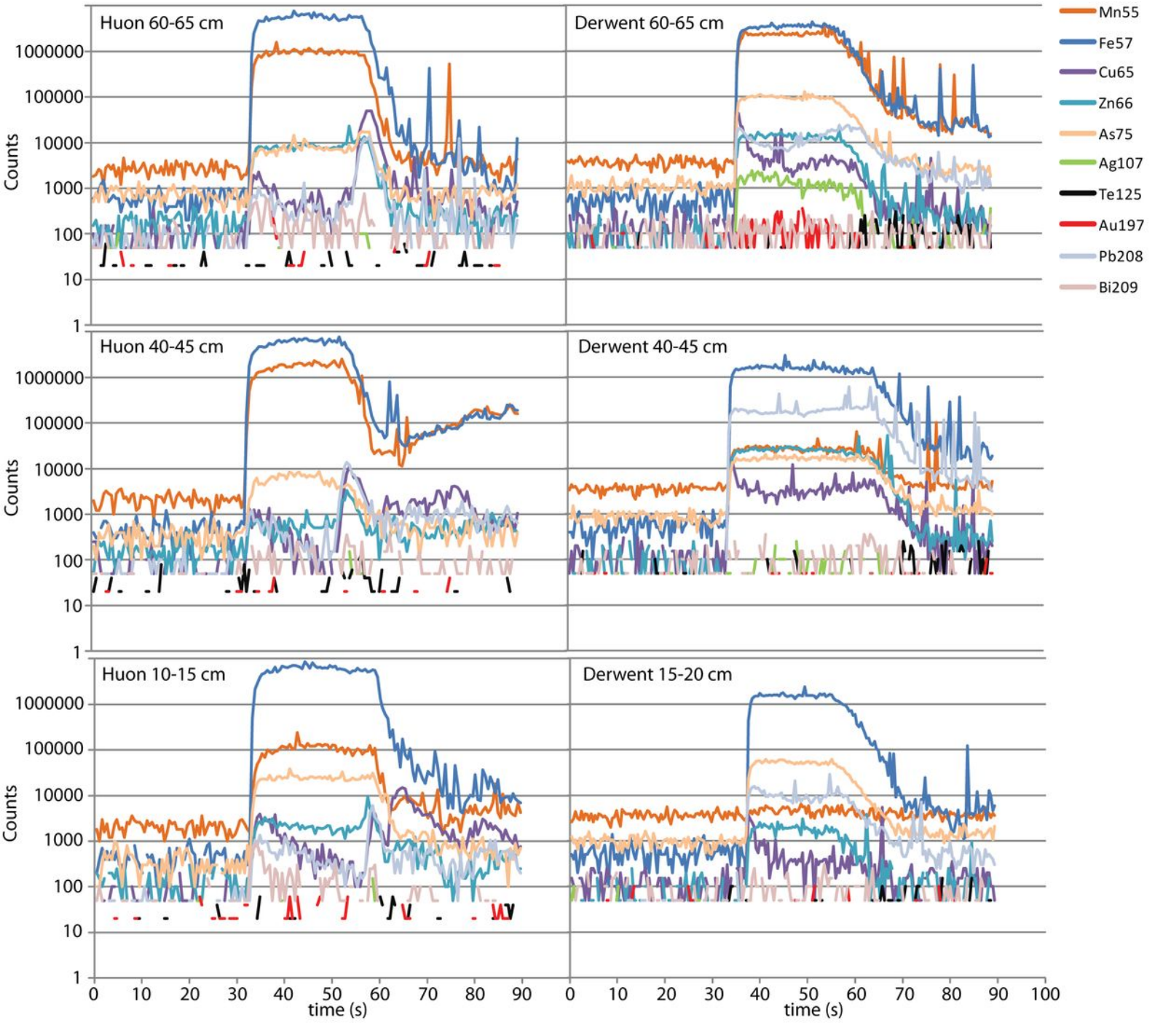
Huon 60-65 cm
Derwent 60-65 cm
Huon 40-45 cm
Derwent 40-45 cm
Huon 10-15 cm
Derwent 15-20 cm
Counts
1000000
100000
10000
1000
100
10
1
0
10
20
30
40
50
60
70
80
90
100
time (s)
Mn55
Fe57
Cu65
Zn66
As75
Ag107
Te125
Au197
Pb208
Bi209

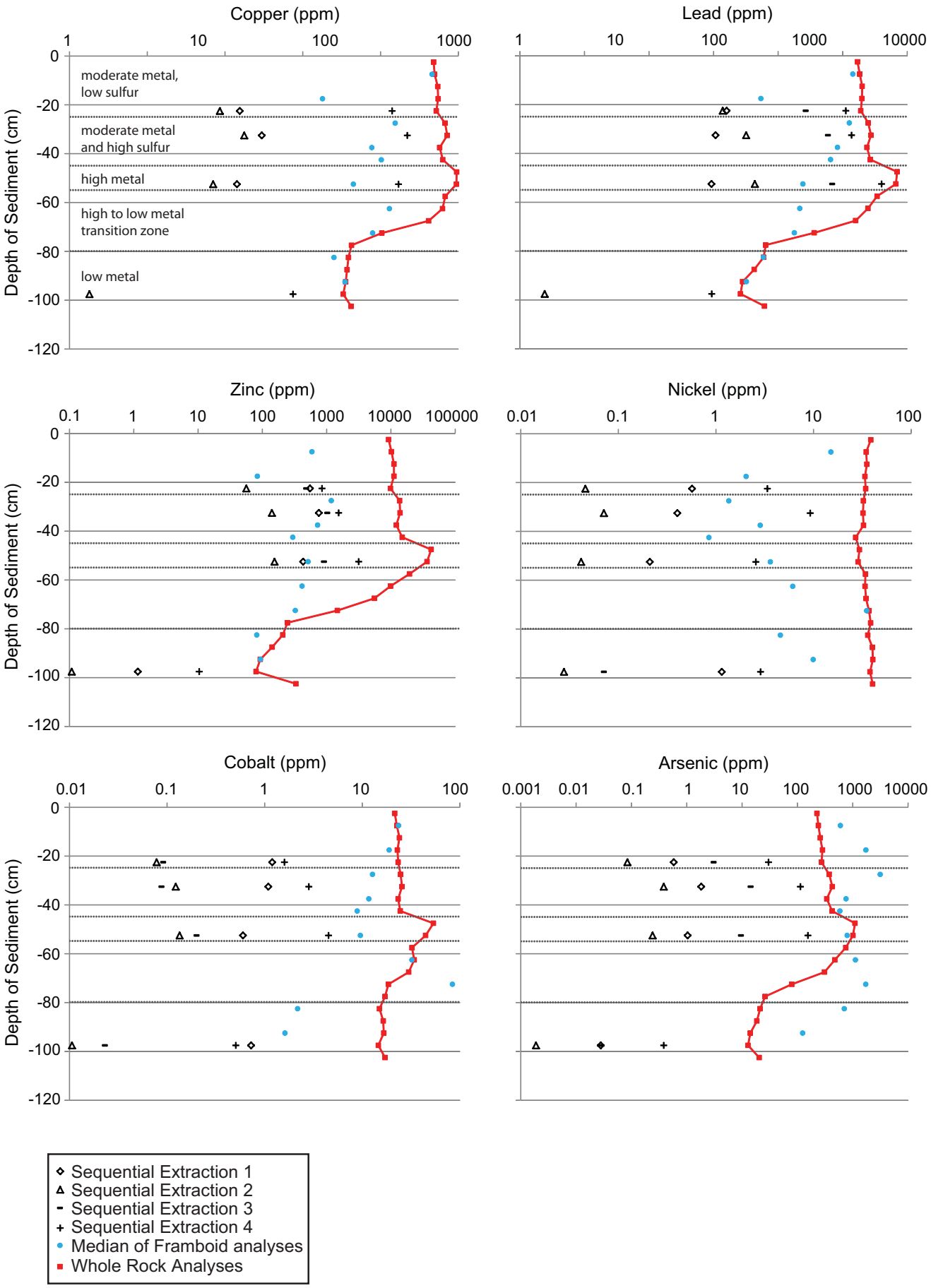
Copper (ppm)
Lead (ppm)
Zinc (ppm)
Nickel (ppm)
Cobalt (ppm)
Arsenic (ppm)
Depth of Sediment (cm)
moderate metal, low sulfur
moderate metal and high sulfur
high metal
high to low metal transition zone
low metal
Sequential Extraction 1
Sequential Extraction 2
Sequential Extraction 3
Sequential Extraction 4
Median of Framboid analyses
Whole Rock Analyses